



Chemical Exchange Saturation Transfer MRI Optimal Continuous Wave RF Irradiation Parameters for Glycogen (glycoCEST) Detection

Gizeaddis Lamesgin Simegn^{1,2} · Ali Alhamud^{2,3,4} · Frances Robertson^{2,3} · Andre J. W. van der Kouwe^{2,5,6}

Received: 25 February 2020 / Revised: 5 May 2020 / Published online: 24 June 2020
© Springer-Verlag GmbH Austria, part of Springer Nature 2020

Abstract

Chemical exchange saturation transfer (CEST) enables detection of molecules such as glycogen, whose concentrations are too low to impact the signal intensity of standard MR imaging. Detection of these molecules is achieved by selectively saturating a molecule of interest and by measuring the reduction in water signal due to saturation transfer. CEST effects are dependent on parameters such as CEST agent concentration, pH, temperature, relaxation rate, magnetic field strength as well as on experimental parameters such as repetition time, RF irradiation amplitude, and the imaging readout scheme. Measurement of molecules with exchangeable protons that resonate very close to water, e.g., hydroxyl groups in glycogen, is challenging especially at lower magnetic field strengths, mainly due to the effect of direct water saturation. Therefore, optimal RF irradiation parameters that maximize the CEST signal and reduce the competing factors are important for better quantification of glycogen-weighted CEST effects. In this study, analytical solution of the Bloch-McConnell equations was used to find optimal continuous wave RF irradiation parameters for detection of glycogen. In vivo tests were performed on a human calf muscle at different saturation powers to validate the optimal saturation parameters determined via simulation. The selected parameters were applied in vitro to CEST measurements in a phantom with varying glycogen concentrations and also in vivo in a human calf muscle. Our results show the possibility of detecting glycogen using CEST MRI at 3 T. It is further shown that the glycoCEST signal can be maximized by optimizing the RF pulse irradiation parameters (duration and power) and that different glycogen concentrations can be identified when applying the optimized saturation pulse.

✉ Gizeaddis Lamesgin Simegn
ltime.et@gmail.com

Extended author information available on the last page of the article

1 Introduction

Glycogen plays a major role in supporting the energy demands of skeletal muscle during prolonged exercise. Quantification of glycogen is important for disease diagnosis (e.g., glycogen storage disorder and skeletal/cardiac myopathy), disease progression monitoring, and therapeutic outcome evaluation in clinical and preclinical settings. Depletion of muscle glycogen also affects exercise performance; however, repletion and depletion are poorly quantified. Currently, glycogen can be measured by invasive tissue sampling through needle biopsy, Positron Emission Tomography (PET) which uses ionizing radiation and ^{13}C magnetic resonance spectroscopy (MRS). Due to the numerous practical disadvantages of measuring glycogen in humans by tissue biopsy and using ionizing radiation, there has been widespread interest in detection of glycogen *in vivo* by ^{13}C MRS in multiple organs, including the heart [1], liver [2], skeletal muscle [3], and brain [4]. With MRS methods, a wide dynamic range of glycogen levels has been observed. However, ^{13}C MRS is available only in specialized research sites and requires costly hardware upgrades and ^{13}C isotopes, not routinely available on clinical MRI scanners [5]. The ability to measure glycogen in different organs non-invasively using standard MRI hardware would be helpful for a wide variety of applications.

Chemical exchange-dependent saturation transfer (CEST) MRI is a recent MRI contrast method that can detect macromolecules, including glycogen, from the nanomolar to millimolar range. Since hydrogen nuclei bound to different molecules and those in free water possess different chemical shifts (i.e., resonance frequencies), MRI methods to probe these exchange processes make use of a spectrally selective excitation of the nuclei in one pool and detection of the attenuated MRI signal in the other pool (bulk water). The exchange of protons between the two pools results in unique contrasts that can be used to quantitatively assess physiological exchange processes, including amide proton transfer (APT) [6], glycosaminoglycan (GAGCEST) [7], and glutamate and γ -aminobutyric acid (GABA) [8]. This also introduces the possibility for indirect detection of glycogen via the MRI water resonance by exploiting chemical exchange between the hydroxyl ($-\text{OH}$) protons and free water. The feasibility of detecting glycogen using CEST (glycoCEST) has previously been demonstrated *in vivo* in animal studies of the liver at 4.7 T [5]. Detection of skeletal muscle glycogen has also been performed at 3 T in different muscle groups using CEST MRI in conjunction with the water saturation shift referencing (WASSR) frequency correction method [9].

To generate CEST signal, a magnetization preparation pulse is embedded in the pulse sequence. One of two RF pulse types can be used to perform the saturation: continuous wave (CW) or pulsed wave (PW). In CW-CEST, a long rectangular RF pulse is used to saturate the metabolite protons, whereas in pulsed-CEST, multiple pulses with short duration are applied [10]. The specific absorption rate (SAR) and hardware limitations determine the choice of pulse type [11]. Although PW saturation helps to reduce the burden on the hardware as well as the SAR level, in practice the optimization of the PW RF pulse is often performed experimentally [12]. The CW RF pulse type is widely used for its simplicity and

ease of optimization, although sequence parameters including saturation irradiation pulse design and readout RF pulse type and duration require consideration [13].

The CEST effect is sensitive to solute proton concentration and exchange rate and also to factors that affect the exchange rate including pH and temperature. However, CEST signal also depends on relaxation rate and magnetic field strength [14]. It has been shown that the apparent CEST measurement varies strongly with experimental parameters such as the RF irradiation amplitude (B_1) and duration [14, 15]. Generally, fast exchanging hydrogen protons (as in glucose and glycogen) are expected to produce good CEST signal only when saturated with high RF power, whereas slower exchanging molecules (like amide groups) require less power. However, SNR is also affected at high saturation power levels.

Magnetization transfer (MT)—transfer of magnetization between semi-solid macromolecules and water, and the direct water saturation (DS) or spillover effect [12] also affect the CEST signal depending on the RF irradiation level. The spillover effect dominates, reducing the observable signal especially close to water [16]. Moreover, strong spillover effects shift the magnetic transfer ratio (MTR) asymmetry profile away from water at the center. Hence, the optimum range of offset frequencies that contain the CEST information depends on the applied saturation power. Precise optimization of saturation power depends on the characteristics of the tissue inspected, including water content, T_1 and T_2 relaxation times, and pH. Recent studies have also shown that the CEST effect depends on experimental factors such as repetition time (TR) and flip angle (FA) [17], which also need to be taken into account. For small molecule contrast agents that have a chemical shift very close to the water resonance frequency, like hydroxy groups in glycogen, the CEST effect is very sensitive to parameter selection, and choosing the saturation parameters that maximize the signal is crucial. Previous studies have used a continuous-wave rectangular RF saturation pulse with a B_1 field strength of 3 μT and duration of 300 ms to detect glycogen in the liver [18] and a B_1 field strength of 0.75 μT , duration 500 ms for skeletal muscle [9]. Although the optimal RF power and duration have not been systematically determined, they are likely to differ between tissues due to differences in T_1 , T_2 , and water content.

Different approaches have been used to optimize the amplitude of RF pulses that maximizes CEST signal [19, 20]. Both analytical and numerical mathematical models have been developed to describe the CEST signal mechanism. However, numerical methods are computationally complex, the insight into the intrinsic structure of Z-spectra is limited, and no analytical optimization for designing experiments is possible.

Despite its broad range of potential applications [6, 7, 21–25], CEST MRI lacks a standard as to which RF pulse type, duration and power, and pulse sequence to use for a specific molecule of interest at a particular magnetic field strength, limiting its use for routine clinical applications. In this study, analytical solution of the Bloch-McConnell (BM) equations were used to analyze the dependence of the glycoCEST effect on CW RF irradiation parameters and to select optimal values that maximize the proton transfer ratio using a 2D single-shot gradient echo EPI sequence at 3 T. This is then validated in vivo and demonstrated on a glycogen phantom.

2 Theory

2.1 Bloch–McConnell (BM) Equations

The Bloch–McConnell equations are two sets of Bloch equations modified with exchange terms between the solute and free water protons that are commonly used to describe proton transfer experiments. Even though the general solution for a broad range of irradiation parameters is complicated, concise results can be derived under certain assumptions [26]. For a typical 2-pool chemical exchange model, comprising pool *a* (the water pool) and pool *b* (the dilute solute pool, glycogen in this case), with forward ($a \rightarrow b$) exchange rate k_a and thermal equilibrium magnetizations $M_{0,a}$ and $M_{0,b}$, in a static magnetic field $B_0 = (0, 0, B_0)$, the ratio $M_{0,b}/M_{0,a}$ is conserved by the backward ($b \rightarrow a$) exchange rate k_a ($M_{0,b}/M_{0,a} = fb/kb$). Pool *a* is the measured pool, which is the spin ensemble of water protons.

On resonance, the RF irradiation field $B_1 = (B_1, 0, 0)$ causes the magnetization to process around the *x*-axis in the rotating frame, with frequency $\omega_1 = \gamma B_1$. For off-resonance irradiation, the magnetization rotates around the effective field $B_{\text{eff}} = (\omega_1, 0, \Delta\omega)/\gamma = \omega_{\text{eff}}/\gamma$ at an angle $\theta = \tan^{-1}(\omega_1/\Delta\omega)$ from the *z* axis. The dynamics of magnetizations of the two pools during off-resonance irradiation is described by the BM equations for the case of exchange between pool *a* and *b* and by the differential equations for dipolar-coupled systems [27]. In the rotating frame of reference (*x*, *y*, *z*), the time-dependent BM equations for two pools, water (pool *a*), CEST (pool *b*) are [28, 29]:

$$\frac{d}{dt}\vec{M} = A \cdot \vec{M} + \vec{C} \quad (1)$$

with the six-dimensional magnetization vector *M*

$$\vec{M} = \begin{pmatrix} M_{xa} \\ M_{ya} \\ M_{za} \\ M_{xb} \\ M_{yb} \\ M_{zb} \end{pmatrix} \quad (2)$$

And a block matrix *A*:

$$A = \begin{bmatrix} L_a - K_a & +K_b \\ +K_a & L_b - K_b \end{bmatrix} \quad (3)$$

consisting of 3×3 submatrices $K_i = k_i \cdot I_i$, and L_i where $i = a, b$

$$L_i = \begin{pmatrix} -R_{2i} & -\Delta\omega_i & 0 \\ +\Delta\omega_i & -R_{2i} & +\omega_1 \\ 0 & -\omega_1 & -R_{1i} \end{pmatrix} \quad (4)$$

And the constant vector *C*:

$$\vec{C} = \begin{pmatrix} 0 \\ 0 \\ R_{1a}M_{0a} \\ 0 \\ 0 \\ R_{1b}M_{0b} \end{pmatrix} \quad (5)$$

$\Delta\omega_a = \omega_{rf} - \omega_a$ is the frequency of the oscillating B_1 field (ω_{rf}) offset relative to the Larmor frequency ω_a of pool a (for ^1H : $\omega_d/B_0 = \gamma = 42.58 \text{ Hz}/\mu\text{T}$). The offset of pool b : $\Delta\omega_b = \omega_{rf} - \omega_b = \Delta\omega_a - \delta_b\omega_a$, is shifted by δ_b parts per million (ppm) relative to the water proton resonance. $R_{1,a/b} = 1/T_{1,a/b}$ and $R_{2,a/b} = 1/T_{2,a/b}$ are longitudinal and transverse relaxation rates.

The exchange rate from free water to solute protons (K_a) can be calculated using the following relationship based on the mass balance between two pools [30]:

$$K_a = f_b K_b = f_b \begin{pmatrix} k_b & 0 & 0 \\ 0 & k_b & 0 \\ 0 & 0 & k_b \end{pmatrix} \quad (6)$$

$$f_b = \frac{M_{0b}}{M_{0a}} = \frac{n_b \cdot [b]}{n_a \cdot [a]}, \quad (7)$$

where f_b is the proton fraction, $[a]$ and $[b]$ are the concentrations and n_a and n_b are the number of protons per molecule for pools a and b . The population fraction f_b can be assumed to be $< 1\%$; hence $k_{ab} < k_{ba}$ [30].

For three pools, pool c for semi-solid macromolecular protons, Eq. (3) transforms to [31]

$$A = \begin{bmatrix} L_a - K_{ab} & +K_{ba} & +K_{ca} & +K_{da} & +K_{fa} \\ +K_{ab} & L_b - K_{ba} & 0 & 0 & 0 \\ +K_{ac} & 0 & L_c - K_{ca} & 0 & 0 \\ +K_{ad} & 0 & 0 & L_d - K_{da} & 0 \\ +K_{ae} & 0 & 0 & 0 & L_e - K_{ea} \end{bmatrix} \quad (8)$$

2.2 Solution of the Bloch–McConnell Equations

The BM equations are first-order ordinary differential equations with an inhomogeneous term (Eq. 1). The formal solution of the BM equations that is commonly used for numerical solution is [28]:

$$\vec{M} = (\vec{M}_0 + A^{-1}\vec{C}) \exp(A \cdot t_{\text{sat}}) - A^{-1}\vec{C} \quad (9)$$

However, this method is computationally complex and does not allow analytical optimization for designing experiments.

The CEST effect is usually analyzed using magnetic transfer ratio asymmetry (MTR_{asym}) obtained from Z-spectra (CEST spectra) plotted as a function of RF irradiation frequency [26, 28]. The Z value after long irradiation at an RF frequency offset $\Delta\omega$ is given by the z component of the water (pool a) magnetization ($M_{za}(\Delta\omega)$) normalized by the equilibrium magnetization (M_{0a}) without RF saturation:

$$Z(\Delta\omega) = \frac{M_{za}(\Delta\omega_a)}{M_{0a}} \quad (10)$$

The proton transfer ratio that excludes effects of direct water saturation and semi-solid macromolecular magnetization transfer (MT) can be analyzed using Z-spectrum asymmetry obtained from saturation of corresponding frequencies $+\Delta\omega$ and $-\Delta\omega$ either side of the water resonance, as follows [26, 28]:

$$MTR_{\text{asym}} = \frac{M_{za}(-\Delta\omega_a) - M_{za}(\Delta\omega_a)}{M_{0a}} = Z(-\Delta\omega) - Z(+\Delta\omega) \quad (11)$$

Using an Eigenspace solution to the Bloch-McConnell equation for two pools, Eq. (10) can be formulated as follows:

$$Z(\Delta\omega) = \frac{\cos^2\theta \cdot R_{1a}}{R_{1p}(\Delta\omega_a)} \quad (12)$$

For two pools, the longitudinal relaxation in the rotating frame R_{1p} is a superposition of water relaxation R_{eff} and exchange dependent relaxation (CEST) R_{cest} [26, 31, 32]:

$$R_{1p}(\Delta\omega) = \underbrace{(R_{1a} \cos^2\theta + R_{2a} \sin^2\theta)}_{R_{\text{eff}}} + \underbrace{\left(f_b k_{ba} \cdot \frac{\omega_1^2}{\omega_1^2 + k_{ba}(k_{ba} + R_{2a})} \right)}_{R_{\text{cest}}} \quad (13)$$

where

$$\sin^2\theta = \frac{\omega_1^2}{(\omega_1^2 + \Delta\omega^2)}; \cos^2\theta = \frac{\Delta\omega^2}{(\omega_1^2 + \Delta\omega^2)} \quad (14)$$

For three pools (water, CEST, and MT) if $f_{b,fc} < 1$, the longitudinal relaxation R_{1p} can be described as follows [31, 32]:

$$R_{1p}(\Delta\omega) = R_{\text{eff}}(\Delta\omega)(\Delta\omega) + R_{mt}(\Delta\omega) + R_{\text{cest}}, \quad (15)$$

where the MT relaxation rate R_{mt} in rotating frame is as follows:

$$R_{mt}(\Delta\omega) = \frac{(\Delta\omega_1^2 + r_{2a}^2) \cdot (k_{ca}r_{1a} + r_{1c}(k_{ac} + r_{1a})) + \omega_1^2 \cdot r_{2a} \cdot (k_{ca} + r_{1c})}{(\Delta\omega_1^2 + r_{2a}^2) \cdot (k_{ca} + k_{ac} + r_{1a} + r_{1c}) + 2 \cdot r_{2a} \cdot (k_{ca}r_{1a} + r_{1c}(k_{ac} + r_{1a})) + \omega_1^2 \cdot (k_{ca} + r_{2a} + r_{1c})} \quad (16)$$

And $r_{1a} = R_{1a} - R_{\text{eff}}$, $r_{2a} = R_{2a} - R_{\text{eff}}$, and $r_{1c} = R_{1c} + R_{1s} - R_{\text{eff}}$.

Zaiss et al. [32] show that considering the effect of semi-solid MT pool c on T_1 recovery time, the relaxation rate R_{1a} in Eq. (12) is $R_{1\text{obs}}$. Since CEST pools have a low relative concentration, the effect of the labile proton pool b can be neglected and $R_{1\text{obs}}$ expressed as follows:

$$R_{1\text{obs}} \approx \frac{R_{1a} + f_c R_{1c}}{1 + f_c} \quad (17)$$

Then from Eq. (12) the adjusted Z-spectrum for three pools is the following:

$$Z_{ss}(\Delta\omega) = \frac{\cos^2\theta \cdot R_{1\text{obs}}}{R_{1p}} \quad (18)$$

The Z-spectrum after RF irradiation of duration t_p is then given by

$$Z(\Delta\omega, t_p) = (\cos^2\theta \cdot Z_i - Z_{ss}) \cdot e^{-R_{1p}t} + Z_{ss}, \quad (19)$$

where Z_i is the initial magnetization before saturation [31, 32]. This allows for optimization of irradiation parameters that maximize the Z-spectrum and hence the MTR_{asym} .

3 Methods

3.1 Simulation

The CEST (Z) spectra for glycoCEST were simulated in Matlab (MathWorks 2014b) using a three-pool exchange model [31]. The dependence of CEST on RF irradiation power and duration was examined. Taking into account the specific absorption rate limit [33], irradiation RF power was simulated between 0 and 4 μT for a fixed pulse duration of 1 s and pulse duration was varied between 10 ms and 3.5 s while power was fixed at 1 μT . From the simulated MTR_{asym} curves, the MTR_{asym} integral was calculated within the glycogen resonance frequency range (between 0.5 and 1.5 ppm down field of water) and examined as a function of irradiation power and pulse duration.

The following parameters were used in the simulation: longitudinal relaxation rate and transverse relaxation rate for water pool $R_{1a} = 0.66 \text{ s}^{-1}$, $R_{2a} = 2 \text{ s}^{-1}$, which is $T_{1a} \approx 1500 \text{ ms}$ and $T_{2a} \approx 500 \text{ ms}$ for skeletal muscle at 3 T [34, 35]. The fraction of exchangeable protons for glycogen has been reported as $n_b \leq 3$ depending on the branching of the glycosyl links [5]. Using $n_b = 3$, proton fraction (f_b) = 0.00135 (using Equation [7 50 mM glycogen in water: $3 \times 50 / (2 \times 55.5 \times 1000) = 0.00135$), exchange rate for glycogen is approximately 1000 s^{-1} at room temperature [5, 36], chemical shift of the glycogen pool = 1 ppm, longitudinal and transversal relaxation rates of pool b are approximately $R_{1b} = 1.1 \text{ s}^{-1}$ ($T_{1b} = 900 \text{ ms}$) and $R_{2b} = 76.9 \text{ s}^{-1}$ ($T_{2b} = 13 \text{ ms}$) [37]. Standard parameters were chosen for MT: $T_{1c} = 1 \text{ s}$, $T_{2c} = 8.7 \text{ }\mu\text{s}$, $f_c = 7.4\%$, $k_{ca} = 66 \text{ s}^{-1}$, $\Delta\omega_c = 0 \text{ ppm}$ [32, 34]. The glycogen hydroxyl proton

resonates between approximately 0.5 and 1.5 ppm down field from water [5], that is, 63.87–191.61 Hz at 3 T. We used 127.74 Hz (1 ppm) down field of water as the glycogen chemical shift signature point to evaluate the optimum irradiation parameters that maximizes the CEST signal.

3.2 CEST Pulse Sequence and Acquisition Parameters

The CEST sequence was implemented by adding a frequency selective continuous wave RF pulse on to a 2D gradient echo single-shot Echo Planar Imaging pulse sequence with a rectangular saturation pulse swept between -383.22 and 383.22 Hz in intervals of 19.16 Hz ($-3:0.15:3$ ppm) with respect to the water resonance frequency.

Figure 1 shows the employed CEST sequence with a continuous wave (CW) RF irradiation of duration (t_p) and power (B_1). Since the 2D EPI image acquisition duration is very small, the repetition time can be assumed to be approximately equal to the saturation time plus relaxation recovery time. Hence, the RF duty cycle of 50% given by t_p/TR was selected for good RF amplifier performance [15].

For both phantom and in vivo acquisitions, a 15-channel Tx/Rx knee coil was used with scanning parameters of: TR 2000 ms, TE 21 ms, 43 offset measurements (including two reference unsaturated measurements). Single slice scans with 5 mm thickness, 64×64 acquisition matrix and 220×220 mm FOV were acquired and analyzed.

3.3 In Vivo Validation

In vivo scans were performed on the calf muscle of two human volunteers on a 3 T Skyra (Siemens, Erlangen, Germany) in accordance with a protocol approved by the Partners Healthcare IRB. All experiments were performed following informed written consent. The experiment was first performed at different saturation powers (0.5 – 4 μ T)

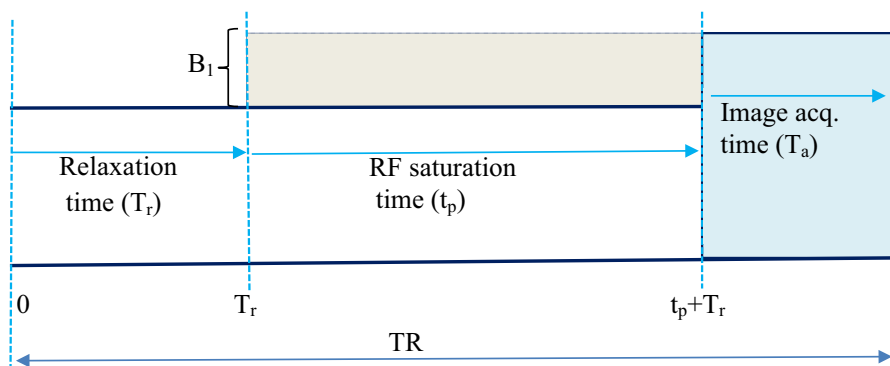


Fig. 1 Illustration of the CEST-EPI pulse sequence. The repetition time (TR) is approximately equal to the sum of recovery time (T_r) and RF saturation time t_p

with a CW pulse duration of 1 s to validate the simulation. This dependence of CEST data on the irradiation duration was not verified experimentally. A second *in vivo* test was performed on a volunteer using the optimized RF irradiation parameters obtained from simulation and *in vivo* validation tests. For this a 1 s CW saturation pulse with power of 1.5 μ T was applied.

3.4 Data Analysis

In vivo curves were generated from a $35 \times 35 \times 5$ mm³ region of interest (ROI) in the inferior part of the gastrocnemius muscle. For all acquisitions, Z-spectra were generated by dividing the ROI average intensity of the saturated images into the ROI average intensity of the reference image. B0 correction was done by fitting the Z-spectra to a polynomial, finding the minimum (which is deemed to be the water frequency) and shifting the minimum towards 0 ppm. The MTR_{asym} curve was then generated by subtracting the intensity of the CEST spectrum down-field of water (positive offset frequencies) from that the spectrum up-field of water (negative offset frequencies). The MTR_{asym} integral was calculated between 0.5 and 1.5 ppm downfield of water (targeting glycogen) from respective MTR_{asym} curves, by adding up the measured points. A custom-written Matlab (MathWorks, Inc 2014) program was used to process the images and generate Z-spectra and MTR_{asym} curves.

3.5 Phantom Test

Five different Bovine liver glycogen (Type IX G0885, CAS Number: 0009005792, Sigma, Aldrich) concentrations (10 mM, 20 mM, 50 mM, 100 mM and 200 mM) mixed with phosphate-Buffered Saline (PBS) solution with a pH of 7 were prepared and tested to demonstrate that the CEST effect changes with different glycogen concentrations at the optimal values of irradiation power and duration selected from the simulation. The concentration of glycogen is expressed in millimolar glycosyl units, with each glycosyl unit contributing 168 g/mol [5]. For example, 100.8 mg of glycogen was dissolved in a 60 ml PBS solution to obtain a 10 mM solution of glycogen ($168 \text{ mg/mmole} \times 0.01 \text{ mol} \times 60 \text{ ml} = 100.8 \text{ mg}$). The phantom scans were performed on a Siemens Skyra 3 T (Erlangen, Germany) scanner at the Athinoula A. Marthinos center for Biomedical Imaging, Massachusetts General Hospital, Boston, USA. The CEST-weighted images for all offsets of each concentration were co-registered to the unsaturated (reference) image and the CEST spectrum was defined as the normalized water intensity (M_{zw}/M_{0w}) as a function of RF saturation frequency or chemical shift.

4 Results

4.1 Simulation

Figure 2 shows the simulated Z-spectra and corresponding MTR asymmetry (MTR_{asym}) spectra as a function of RF irradiation power and duration. Spectral widening can be observed as either saturation power or duration increases.

The z magnetization is attenuated (saturated) with increasing saturation power. Changing pulse duration has less of an effect on CEST spectra than varying saturation power; the effect of saturation (spectral widening) approaches a steady state with further increase in saturation power. A similar effect is observed in the MTR_{asym} curves (Fig. 2b, d). At lower saturation powers (0–1.5 μT) the MTR_{asym} peak shifts towards 1 ppm. However, with a further increase in saturation power there is a line broadening and loss of the CEST effect. Figure 3 shows the simulated MTR_{asym} integral values calculated between 0.5 and 1.5 ppm as a function of irradiation power and irradiation pulse duration. The simulated MTR_{asym} integral

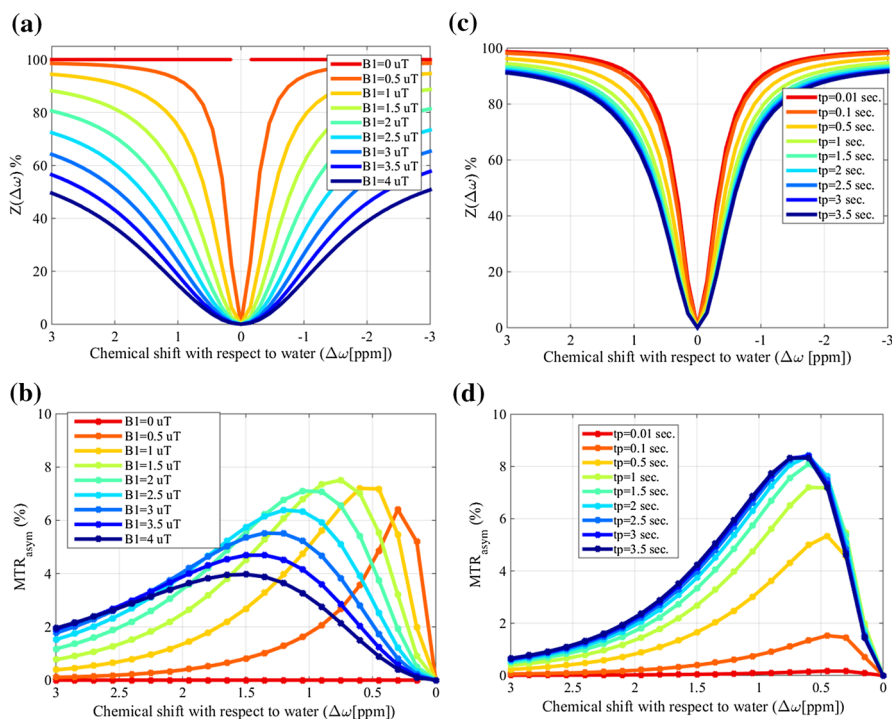


Fig. 2 Simulated Z-spectra (top, **a**, **c**) and MTR_{asym} curves (bottom, **b**, **d**) as a function of irradiation power (B_1) (left, **a**, **b**) and irradiation pulse duration (right, **c**, **d**). A strong dependence of the CEST effect on saturation power is observed in both MTR_{asym} curves and CEST spectra. Relatively slow CEST effect variations are observed at longer saturation durations. Irradiation power and duration were fixed at 1 μT and 1 s, respectively, when duration/power was varied

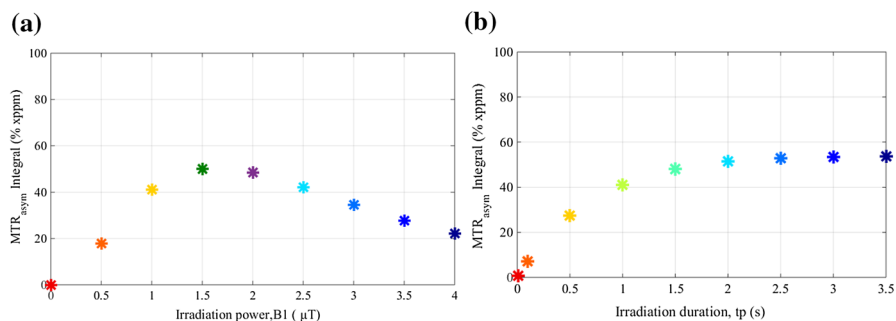


Fig. 3 Simulated MTR_{asymp} integral values calculated between 0.5 and 1.5 ppm as a function of **a** irradiation power and **b** irradiation pulse duration. The integrated MTR_{asymp} shows maximum value at 1.5 μ T RF power and a stable value beyond 2 s saturation duration

increases towards a maximum at a saturation power of 1.5 μ T, decreasing at higher saturation powers. The MTR_{asymp} integral value also increases with increasing RF irradiation duration, levelling off at durations longer than ~ 2 s (Fig. 3b).

4.2 In Vivo Test

Figure 4 shows Z-spectra and corresponding MTR_{asymp} curves from in vivo tests at different saturation powers. In agreement with the simulation, a widening effect can be seen in the CEST spectrum with increasing saturation power. Table 1 shows that the MTR_{asymp} integral calculated between 0.5 and 1.5 ppm gradually increases with increasing irradiation power and decreases after reaching a maximum value at 1.5 μ T.

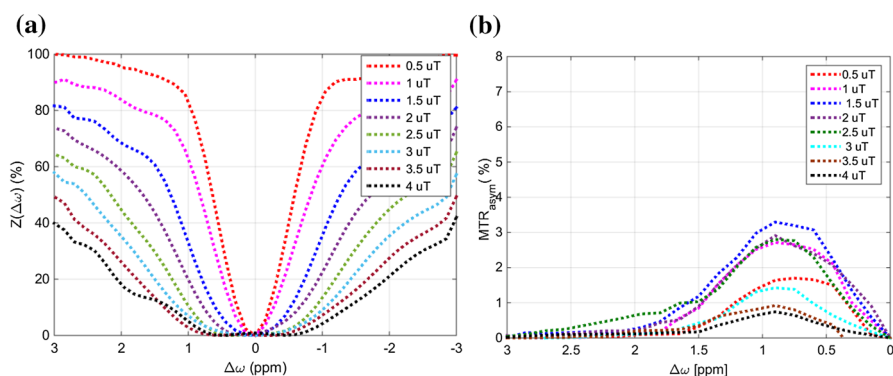


Fig. 4 Z-spectra **(a)** and MTR_{asymp} curves **(b)** from a calf muscle of a single volunteer acquired at different saturation powers. A widening effect in the Z-spectra is observed as the saturation power increases. Highest peak values are seen in the MTR_{asymp} curve at 1.5 μ T. The Z-spectra were generated by fitting a 30th order polynomial to the measure data. Then the MTR_{asymp} curves were generated from the fitted Z-spectrum (by subtracting the fitted signal on either side of 0 ppm)

Table 1 MTR_{asym} integrals between 0.5 and 1.5 ppm as a function of saturation power for in vivo acquisition on a calf muscle. The integral under the fitted MTR_{asym} curve was calculated to find MTR_{asym} integrals

| Saturation power, B1 (μT) | MTR_{asym} integral |
|--|------------------------------|
| 0.5 | 10.31 |
| 1 | 17.74 |
| 1.5 | 21.17 |
| 2 | 18.04 |
| 2.5 | 17.33 |
| 3 | 7.98 |
| 3.5 | 5.12 |
| 4 | 3.98 |

Figure 5 demonstrates the theoretical predictions of the model as a function of saturation power compared to the experimental data. The in vivo data demonstrates the dependence of the weighted glycoCEST relative concentration of the specific muscle group of specific patients on irradiation power while the simulation shows the general dependence. Hence, the predicted MTR_{asym} integral values may not be equal to the experimental data. However, the correlation between the two clearly shows how MTR_{asym} integral is affected by saturation power. On both cases, the optimum saturation power is found to be 1.5 μT .

Figure 6 shows the CEST and MTR_{asym} curves for the calf muscle scan of a second volunteer acquired at the selected optimal irradiation parameters (1.5 μT saturation power and 1 s saturation duration). The “peak” at around 0.9 ppm in the MTR_{asym} curve demonstrates the detection of the glycogen-weighted signal using the selected irradiation parameters.

Figure 7 shows CEST images acquired using the selected optimal saturation power and duration (left to right) without saturation, after saturation at 1 ppm and the MTR_{asym} map overlaid on the reference image. The saturated image displays lower intensity due to the CEST effect.

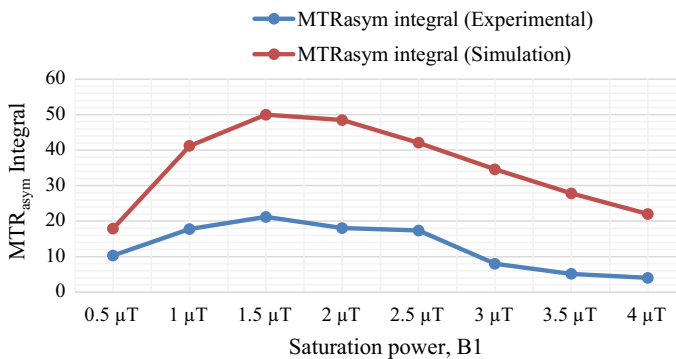


Fig. 5 A plot of simulated MTR_{asym} integrals compared to experimental data as a function of saturation power

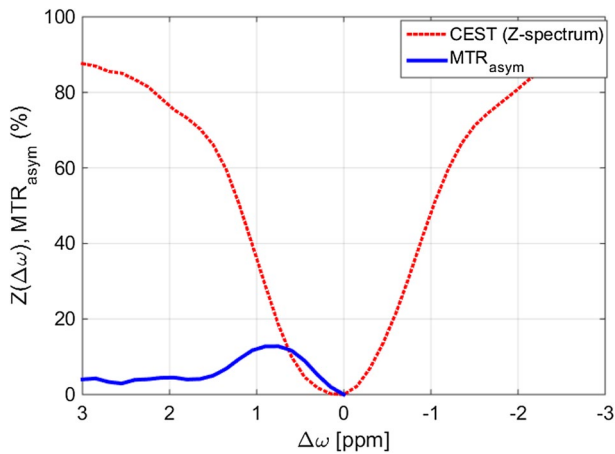


Fig. 6 CEST spectrum and MTR_{asym} curve of the in vivo test for a single volunteer acquired from the inferior part of the gastrocnemius muscle. The Z-spectrum was generated by fitting a 30th order polynomial to the measure data. Then the MTR_{asym} curve were generated from the fitted Z-spectrum (by subtracting the fitted signal on either side of 0 ppm)

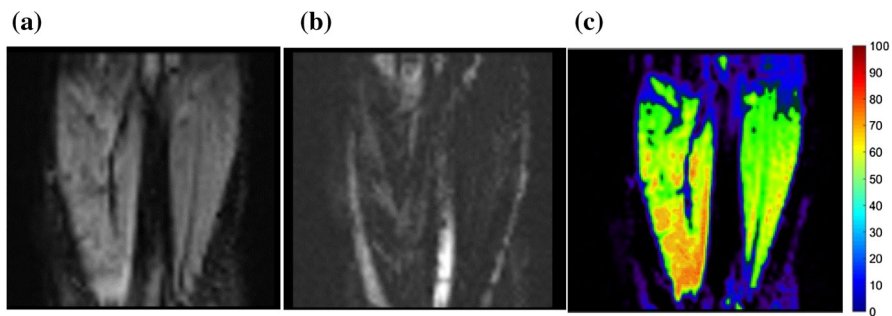


Fig. 7 glycoCEST imaging of human calf muscle **a** unsaturated image, **b** saturated image at 1 ppm, and **c** color-coded MTR_{asym} map at 1 ppm overlaid on the reference image

4.3 Phantom Test

The calculated maps of MTR_{asym} at 1 ppm for five different glycogen phantom concentrations overlaid on the reference image (Fig. 8) demonstrate the ability to detect glycogen-weighted signal using optimized RF saturation parameters for CEST at 3 T. In the MTR_{asym} maps at 1 ppm from water a slight intensity increase can be observed with increasing glycogen concentration.

Figure 9 shows the CEST and corresponding MTR_{asym} curves for five different glycogen concentrations, also demonstrating a larger CEST effect with increasing glycogen concentration.

Table 2 shows the MTR_{asym} integral between 0.5 and 1.5 ppm and peak values at 1 ppm as a function of glycogen concentration. The MTR_{asym} integral and

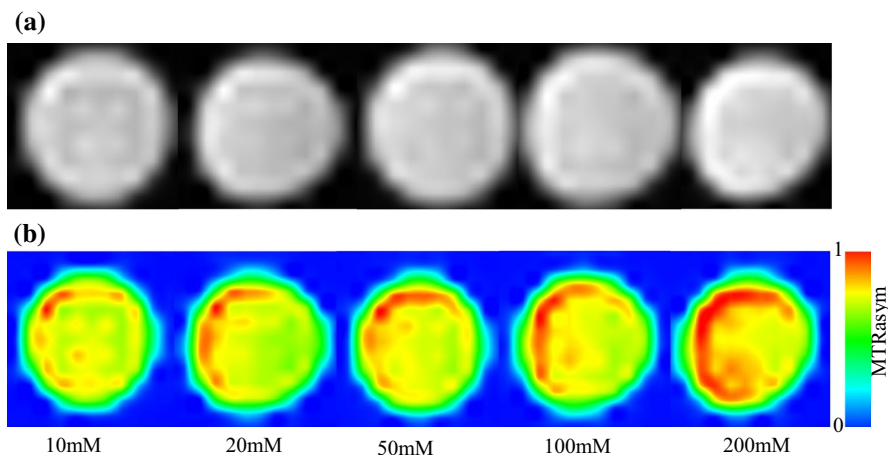


Fig. 8 Phantom scan images of different glycogen concentration levels. **a** Saturated images at 1 ppm. **b** MTR_{asym} maps of glycogen phantom images at 1 ppm overlaid with the reference image

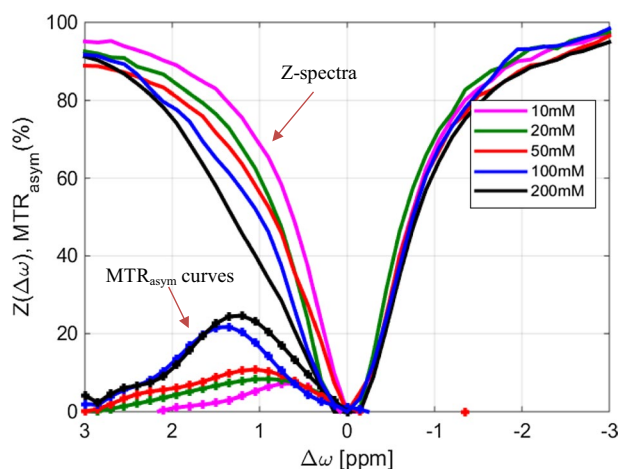


Fig. 9 CEST-spectra and MTR_{asym} curves of glycogen phantom tests at different concentration levels. The Z-spectra were generated by fitting a 30th order polynomial to the measure data. Then the MTR_{asym} curves were generated from the fitted Z-spectrum (by subtracting the fitted signal on either side of 0 ppm)

peak values show a significant linear correlation (Pearson's $r=0.98$ and 0.98 , respectively, both p 's < 0.05) with glycogen concentration. This is also demonstrated in Fig. 10.

Table 2 MTR_{asym} peak values and MTR_{asym} integral between 0.5 and 1.5 ppm for glycogen phantom tests of different concentrations level showing a monotonic increasing correlation with glycogen concentration

| Concentration (mM) | MTR_{asym} peak (max. 0.5–1.5 ppm) | MTR_{asym} integral (0.5–1.5 ppm) |
|--------------------|---|--|
| 10 | 5.18 | 36.95 |
| 20 | 8.34 | 53.55 |
| 50 | 10.33 | 65.75 |
| 100 | 17.46 | 104.32 |
| 200 | 23.19 | 139.18 |

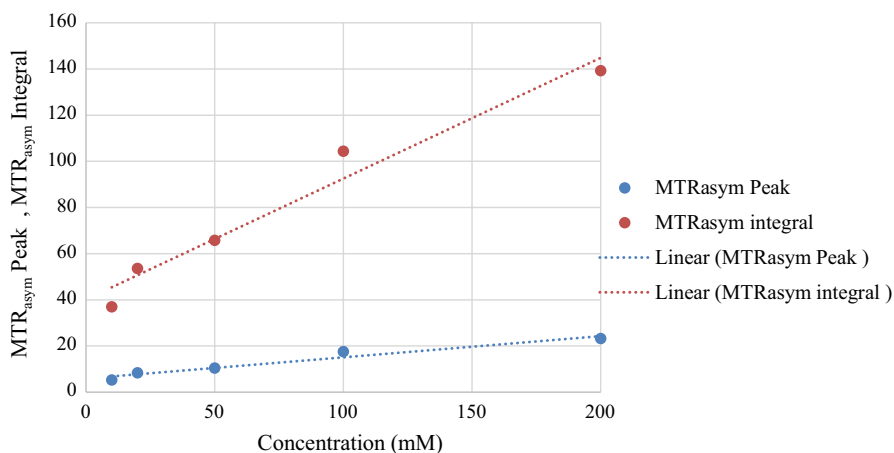


Fig. 10 Correlation plot of MTR_{asym} peak and MTR_{asym} integral values with respect to glycogen phantom concentrations

5 Discussion

Although CEST MRI is a promising technique to detect dilute CEST agents and microenvironmental properties, experimental measurement of the CEST effect is complex due to its dependence not only on CEST agent concentration but also on experimental parameters such as scanner field strength, RF irradiation amplitude and duration, pulse sequence and image acquisition scheme. Detecting glycogen using CEST MRI is more challenging due to its close resonance with free water, which makes it more likely to be contaminated by direct water saturation (spillover effect) and other CEST pools resonating at overlapping frequencies due to smaller absolute chemical shift [18]. This is especially problematic at lower magnetic field strengths, such as 3 T, where the sensitivity of CEST signals substantially decreases compared to high and ultra-high magnetic fields (> 7 T) [38].

However, an optimal irradiation power and saturation duration can be selected by balancing saturation efficiency, direct water saturation and MT [38–40] to maximize the measurable CEST effect.

Weak power causes inefficient labile proton saturation leading to an attenuated CEST effect; on the other hand, very strong RF power directly attenuates the bulk water signal (in addition to saturating the solute protons), reducing the sensitivity and specificity of CEST [14, 23, 41].

As demonstrated in the simulated Z-spectrum (Figs. 2 and 3), very weak irradiation power ($< 0.5 \mu\text{T}$) causes saturation efficiency for the solute resonance to be low, and the water signal reduction due to saturation transfer is small. The saturation efficiency increases gradually with the applied irradiation power and reaches its optimal value ($\approx 1.5 \mu\text{T}$), correspondingly reducing the water proton signal. On the other hand, strong saturation power ($> 2.5 \mu\text{T}$) introduces additional spillover effects, thus reducing proton transfer ratio as reflected by the MTR_{asym} curve at the glycogen proton frequency ($\approx 1 \text{ ppm}$) (Fig. 2b).

The simulated MTR_{asym} integral also increases asymptotically towards a maximum at durations longer than $\sim 2 \text{ s}$ (Fig. 3b), reflecting the steady-state proton exchange between solute and water pool where further irradiation is not required. As saturation duration increases, higher saturation is accumulated and a larger CEST effect is seen compared to short durations. The simulation results confirm the dependence of MTR_{asym} on RF saturation power and duration, identifying a maximum MTR_{asym} peak at a power of $1.5 \mu\text{T}$, with a pulse duration of 1 s . Only an incremental gain in MTR_{asym} peak is achieved beyond 1 s .

In agreement with the theory and simulation, in the *in vivo* experiment a widening effect is seen in the CEST spectrum when saturation power is increased (Fig. 4). Even though the MTR_{asym} curves plotted as a function of saturation power do not exactly mirror the results obtained via simulation (compare Fig. 3), the peak MTR_{asym} is also seen for an acquisition with $1.5 \mu\text{T}$ saturation power. The MTR_{asym} integral calculated between 0.5 and 1.5 ppm (Table 1), also shows a maximum at $1.5 \mu\text{T}$, with lower and higher irradiation powers resulting in smaller values of MTR_{asym} , as expected.

Overall, the simulations and *in vivo* tests show that for a continuous wave CEST experiment, using a 2D gradient echo single shot EPI pulse sequence, hydroxyl protons are more sensitive to approximately $1\text{--}2 \mu\text{T}$ irradiation power, and longer saturation durations ($1\text{--}2.5 \text{ s}$) are desirable to achieve maximal CEST signal. The specific absorption rate limit during *in vivo* tests [33] restricts the irradiation duration. Hence a 1-s irradiation duration, which results in a 50% duty cycle as recommended [15] was selected as an optimal value for our test. However, this can be increased by selecting a longer repetition time (TR) at the cost of extending scanning time.

Because glycogen hydroxyl protons resonate close to the water resonance frequency and since their proton exchange is intermediate to fast in the MR time scale, they are not visible in a standard proton spectrum under physiological conditions [5], especially at lower magnetic fields. Hence, “suppression” or “dips” around the expected glycogen resonance are not directly observable in the CEST spectrum. However, peaks in the MTR_{asym} curves between 0.75 and 1.2 ppm are evidence of glycogen hydroxyl proton exchange and are more prominent at higher glycogen concentrations (Fig. 8). In human calf muscle, strong diamagnetic CEST effects have been observed at around $1.5\text{--}2 \text{ ppm}$, especially at higher field strengths. These effects have been attributed to the exchangeable

protons of creatine or phosphocreatine [42, 43]. While such effects are not clear in our data obtained at 3 T, small effects were observed in the Z-spectra of Fig. 4 at around 2 ppm with high irradiation power (especially 4 μ T).

Higher glycogen phantom concentrations result in asymmetric broadening of the Z-spectrum. Correspondingly, an increase in signal intensity with increasing glycogen concentrations was apparent in the MTR_{asym} maps at 1 ppm overlaid on the reference image (Fig. 6). The amount of saturation depends on the proton exchange rate and concentration, and saturation efficiency can only approach a maximum of 100% which may be reached at lower concentrations and higher exchange rates [5]. Hence the magnitude of the CEST effect may not scale linearly with concentration. However, phantom test results in Table 2 show that MTR_{asym} integral has a significant correlation ($r=0.981$, $p<0.05$) with glycogen concentration. This is also demonstrated in Fig. 10 correlation plot. Although MTR_{asym} integral values do not represent absolute glycogen concentrations, this confirms that they can be used as glycogen-weighted values for comparative analysis, including longitudinal studies, perfusion studies, or muscle glycogen depletion–repletion studies in sports physiology.

The principle of endogenous glycogen CEST (glycoCEST) imaging was first demonstrated by van Zijl et al. [5] in the excised perfused mouse liver at 4.7 T. Other studies have been conducted to study the distribution of glucose in mouse livers at 4.7 T using a PARACEST sensor [44], at 9.4 T using CEST [45]. In vivo studies of glycogen in humans are limited and only a few have been performed at 3 T [9, 18]. In agreement with the literature, a higher peak at around 0.9 to 1 ppm in the MTR_{asym} curve was observed in our in vivo test on a human calf muscle demonstrating the detection of glycogen-weighted signal using the selected irradiation parameters at 3 T (Fig. 6). The image acquired after applying saturation (Fig. 7b) displays lower intensity because of the CEST effect from presaturation at 1 ppm. The MTR_{asym} map (Fig. 7c) shows regions where there is a strong CEST-weighted effect, presumably showing regions of the imaged calf muscle where glycogen storage is highest. The in vivo test results demonstrate the possibility of detecting glycogen hydroxyl protons at 3 T using optimized irradiation parameters.

Further work could assess the dependence of the glycoCEST effect on read-out RF pulse flip-angle and pulse sequence type. An increase in temperature increases the exchange rate of hydroxyl protons reducing its visibility in the proton NMR spectra. Interestingly, it was shown that, at high temperature the detection sensitivity of glycogen is enhanced in the CEST-spectra due to the dependency of the CEST effect on the proton exchange rate [46, 47]. The optimized parameters in the paper are based on a glycogen exchange rate of 1000 s^{-1} (approximate rate at room temperature). This best served to identify glycogen phantoms with different concentration levels. However, more accurate optimization and detection of glycogen in vivo could be obtained by performing the simulation and optimization at physiological parameters.

6 Conclusion

Given that the concentration of certain endogenous molecules is very low, detection using the CEST method requires optimization of experimental parameters to maximize the CEST effect and reduce competing factors. Along with the B_0 magnetic field strength, RF irradiation parameters play a determining role in the size of the observable CEST effect. In this study, analytical solution of the Bloch-McConnell equations was used to find the optimal RF irradiation power and duration that maximize the glycoCEST weighted signal, and they were found to be 1.5 μT and 1 s, respectively, for the 2D gradient echo ss-EPI pulse sequence. In vivo tests were performed at different RF saturation powers to validate the simulation results. Further phantom and in vivo test results demonstrate the ability of the optimized CEST MRI sequence to detect and measure different concentrations of glycogen at 3 T. This ability to non-invasively measure muscle glycogen using CEST MRI has the potential to advance our understanding of glycogen metabolism in sports physiology, as well in glycogen related disorders.

Acknowledgements Resources necessary for the study were provided by Athinoula A. Martinos Center for Biomedical Imaging/Massachusetts General Hospital, University of Cape Town Medical Imaging Research Unit, Cape Universities Body Imaging Centre and School of Biomedical Engineering, Jimma Institute of Technology, Jimma University. The study was supported by the Netherlands Initiative for Capacity development in Higher Education-NICHE/ETH/247 Project, University of Cape Town international travel award, NRF/DST South African Research Chairs Initiative, NRF Thuthuka grant TTK 150612119380, and NIH grants R01HD071664, R01HD085813, R21MH108346.

References

1. P.A. Bottomley, C.J. Hardy, P.B. Roemer, O.M. Mueller, *Magn. Reson. Med.* **12**(3), 348–363 (1989)
2. I. Magnusson, D.L. Rothman, L.D. Katz, R.G. Shulman, G.I. Shulman, *J. Clin. Investig.* **90**(4), 1323–1327 (1992)
3. G.W. Cline, K.F. Petersen, M. Krssak, J. Shen, R.S. Hundal, Z. Trajanoski, S. Inzucchi, A. Dresner, D.L. Rothman, G.I. Shulman, N. Engla, *J. Med.* **341**(4), 240–246 (1999)
4. G. Oz, P.G. Henry, E.R. Seaquist, R. Gruetter, *Neurochem. Int.* **43**(4–5), 323–329 (2003)
5. V. Zijl, C.K. Jones, J. Ren, C.R. Malloy, A.D. Sherry, *Proc. Natl. Acad. Sci. USA* **104**(11), 4359–4364 (2007)
6. J. Zhou, B. Lal, D.A. Wilson, J. Laterra, P.C.M. van Zijl, *Magn. Reson. Med.* **50**(6), 1120–1126 (2003)
7. W. Ling, R.R. Regatte, G. Navon, A. Jerschow, *Proc. Natl. Acad. Sci. USA* **105**(7), 2266 (2008)
8. K. Cai, M. Haris, A. Singh, F. Kogan, J.H. Greenberg, H. Hariharan, J.A. Detre, R. Reddy, *Nat. Med.* **18**(2), 302–306 (2012)
9. M. Kim, J. Gillen, B.A. Landman, J. Zhou, P.C.M. van Zijl, *Magn. Reson. Med.* **61**(6), 1441–1450 (2009)
10. G. Liu, Ph.D. Thesis, Case Western Reserve University, Cleveland, Ohio, 2008. 194 p.
11. E. Vinogradov, A.D. Sherry, R.E. Lenkinski, *J. Magn. Reson.* **229**, 155–172 (2013)
12. B. Wu, G. Warnock, M. Zaiss, C. Lin, M. Chen, Z. Zhou, L. Mu, D. Nanz, R. Tuura, G. Delso, *EJN-MMI Physics* **3**(1), 19 (2016)
13. S.-M. Huang, M.-L. Jan, H.-C. Liang, C.-H. Chang, Y.-C. Wu, S.-Y. Tsai, F.-N. Wang, *Sci. Rep.* **5**, 15062 (2015)
14. J. Kim, Y. Wu, Y. Guo, H. Zheng, P.Z. Sun, *Contrast Media Mol. Imaging* **10**(3), 163–178 (2015)

15. W. Jiang, I.Y. Zhou, L. Wen, X. Zhou, P.Z. Sun, *Contrast Media Mol. Imaging* **11**(5), 415–423 (2016)
16. T. Michael, A.A.G. McMahon, W. Jeff, M. Bulte, C.M.P. van Zijl, *Chemical Exchange Saturation Transfer Imaging: Advances and Applications* (Pan Stanford Publishing Pte. Ltd., Singapore, 2017), p. 496
17. P.Z. Sun, J. Lu, Y. Wu, G. Xiao, R. Wu, *Phys. Med. Biol.* (2013). <https://doi.org/10.1088/0031-9155/1058/1017/N1229>
18. M. Deng, S.-Z. Chen, J. Yuan, Q. Chan, J. Zhou, Y.-X.J. Wang, *Mol. Imaging Biol.* **18**(2), 274–282 (2016)
19. P. Zhe Sun, T. Benner, A. Kumar, A.G. Sorensen, *Magn. Reson. Med.* **60**(4), 834–841 (2008)
20. P.Z. Sun, *J. Magn. Reson.* **202**(2), 155 (2010)
21. K.M. Ward, A.H. Aletras, R.S. Balaban, *J. Magn. Reson.* **143**(1), 79–87 (2000)
22. J. Zhou, J.O. Blakeley, J. Hua, M. Kim, J. Laterra, M.G. Pomper, P.C. van Zijl, *Magn. Reson. Med.* **60**(4), 842–849 (2008)
23. P.Z. Sun, A.G. Sorensen, *Magn. Reson. Med.* **60**(2), 390–397 (2008)
24. F.A. Nasrallah, G. Pages, P.W. Kuchel, X. Golay, K.H. Chuang, *J. Cereb. Blood Flow Metab.* **33**(8), 1270–1278 (2013)
25. T. Jin, H. Mehrens, K.S. Hendrich, S.-G. Kim, *J. Cereb. Blood Flow Metab.* **34**(8), 1402–1410 (2014)
26. P.Z. Sun, P.C.M. van Zijl, J. Zhou, *J. Magn. Reson.* **175**(2), 193–200 (2005)
27. R.M. Henkelman, X. Huang, Q.-S. Xiang, G.J. Stanisz, S.D. Swanson, M.J. Bronskill, *Magn. Reson. Med.* **29**(6), 759–766 (1993)
28. K. Murase, N. Tanki, *Magn. Reson. Imaging* **29**(1), 126–131 (2011)
29. D.E. Woessner, S. Zhang, M.E. Merritt, A.D. Sherry, *Magn. Reson. Med.* **53**(4), 790–799 (2005)
30. M. Zaiss, P. Bachert, *Phys. Med. Biol.* **58**(22), R221–269 (2013)
31. M. Zaiss, P. Bachert, *NMR Biomed.* **26**(5), 507–518 (2013)
32. M. Zaiss, Z. Zu, J. Xu, P. Schuenke, D.F. Gochberg, J.C. Gore, M.E. Ladd, P. Bachert, *NMR Biomed.* **28**(2), 217–230 (2015)
33. K.J. Acheson, Y. Schutz, T. Bessard, K. Anantharaman, J.P. Flatt, E. Jequier, *Am. J. Clin. Nutr.* **48**(2), 240–247 (1988)
34. G.J. Stanisz, E.E. Odobina, J. Pun, M. Escaravage, S.J. Graham, M.J. Bronskill, R.M. Henkelman, *Magn. Reson. Med.* **54**(3), 507–512 (2005)
35. G.E. Gold, E. Han, J. Stainsby, G. Wright, J. Brittain, C. Beaulieu, *Am. J. Roentgenol.* **183**(2), 343–351 (2004)
36. E. Liepinsh, G. Otting, *Magn. Reson. Med.* **35**(1), 30–42 (1996)
37. J. Weis, J. Kullberg, H. Ahlström, *J. Magn. Reson. Imaging* **47**(2), 410–417 (2018)
38. G. Liu, X. Song, K.W.Y. Chan, M.T. McMahon, *NMR Biomed.* **26**(7), 810–828 (2013)
39. P.Z. Sun, J. Zhou, J. Huang, P. van Zijl, *Magn. Reson. Med.* **57**(2), 405–410 (2007)
40. K.L. Desmond, G.J. Stanisz, *Magn. Reson. Med.* **67**(4), 979–990 (2012)
41. P.Z. Sun, E. Wang, J.S. Cheung, X. Zhang, T. Benner, A.G. Sorensen, *Magn. Reson. Med.* **66**(4), 1042–1048 (2011)
42. F. Kogan, M. Haris, C. Debrosse, A. Singh, R.P. Nanga, K. Cai, H. Hariharan, R. Reddy, *J. Magn. Reson. Imaging* **40**(3), 596–602 (2014)
43. L. Chen, P.B. Barker, R.G. Weiss, P.C.M. van Zijl, J. Xu, *Magn. Reson. Med.* **81**(1), 69–78 (2019)
44. J. Ren, R. Trokowski, S. Zhang, C.R. Malloy, A.D. Sherry, *Magn. Reson. Med.* **60**(5), 1047–1055 (2008)
45. K. Sagiya, S. Zhang, I. Dimitrov, A. Dean Sherry, M. Takahashi (2014) In proceedings of the 2014 joint annual meeting of International society of Magnetic Resonance in Medicine and European Society for Magnetic Resonance in Medicine and Biology (ISMRM-ESMRMB) (Milan, Italy 10–16 May 2014) Paper 0762
46. P.C.M. van Zijl, C.K. Jones, J. Ren, C.R. Malloy, A.D. Sherry, *Proc. Natl. Acad. Sci. USA* **104**(11), 4359–4364 (2007)
47. P.C.M. van Zijl, N.N. Yadav, *Magn. Reson. Med.* **65**(4), 927–948 (2011)

Affiliations

Gizeaddis Lamesgin Simegn^{1,2}  · **Ali Alhamud**^{2,3,4} · **Frances Robertson**^{2,3} · **Andre J. W. van der Kouwe**^{2,5,6}

¹ School of Biomedical Engineering, Jimma Institute of Technology, Jimma University, Jimma, Ethiopia

² UCT Medical Imaging Research Unit, Division of Biomedical Engineering, Department of Human Biology, University of Cape Town, Cape Town, South Africa

³ Cape Universities Body Imaging Centre (CUBIC), Cape Town, South Africa

⁴ The Al-Amteaz Centre for MRI Solution and Development, Tripoli, Libya

⁵ Athinoula A. Martinos Center for Biomedical Imaging/MGH, Charlestown, MA, USA

⁶ Department of Radiology, Harvard Medical School, Boston, MA, USA